Enhanced oxidation ability of g-C$_3$N$_4$ photocatalyst via C$_{60}$ modification

Xiaojuan Bai [a], Li Wang [a], Yajun Wang [b], Wenqing Yao [a], Yongfa Zhu [a],*

[a] *Department of Chemistry, Beijing Key Laboratory for Analytical Methods and Instrumentation, Tsinghua University, Beijing 100084, China*
[b] *National Center for Nanoscience and Technology, Beijing 100190, China*

ARTICLE INFO

ABSTRACT

C$_{60}$ modified graphitic carbon nitride (g-C$_3$N$_4$) composite photocatalysts C$_{60}$/g-C$_3$N$_4$ were prepared by a facile thermal treatment at 550 °C in atmosphere involving polymerization of dicyandiamide in the presence of C$_{60}$ without adding any other reagent. By incorporating C$_{60}$ into the matrix of g-C$_3$N$_4$, the valance band (VB) of g-C$_3$N$_4$ shifts to lower energy position, and thus gives a strong photo-oxidation capability under visible light. The as-prepared sample shows enhanced degradation of phenol and methylene blue (MB) under visible light ($\lambda > 420$ nm). The C$_{60}$/g-C$_3$N$_4$ composites present considerably high photocatalytic degradation activities on phenol and MB, as well as photocurrent response, under visible light irradiation. They are about 2.9, 3.2 and 4.0 times as high as those of bulk g-C$_3$N$_4$, respectively. Such greatly enhanced photocatalytic activity was originated from the holes and $\bullet$OH, which can be ascribed to strong interaction of conjugative π-bond between C$_{60}$ and g-C$_3$N$_4$.

© 2014 Elsevier B.V. All rights reserved.

1. Introduction

Photocatalysis has been widely applied as removal technique for refractory organic pollutants such as organic dyes and benzene-based organics [1]. Up to date, the majority of research on photocatalytic oxidation technologies is focused on dye/TiO$_2$ system [2–4]. However, the development of efficient, sustainable, visible-light-responsive photocatalytic materials remains a significant challenge. Photocatalysts be capable of mineralization and ring opening for benzene-based series is limited because of the high valance band (VB) position. Therefore, it is urgent to develop efficient photocatalysts that can possess a strong photooxidation capability. Recently, Wang et al. [5] reported that a metal-free polymeric photocatalyst, graphitic carbon nitride (g-C$_3$N$_4$), showed a good photocatalytic performance for hydrogen or oxygen product via water splitting under visible-light irradiation. This easily available organocatalyst features a semiconductor band gap of 2.7 eV corresponding to an optical wavelength of 460 nm [6]. The *tri-s*-triazine ring structure and the high condensation make the polymer possess high stability with respect to thermal (up to 600 °C in air) and chemical attacks (e.g., acid, base, and organic solvents). With an appealing electronic structure, a medium band gap, g-C$_3$N$_4$ is an indirect semiconductor and is valuable for photocatalysis-driven applications [7,8]. The bottom of the conduction band (CB) of

g-C$_3$N$_4$ is located at about -1.3 V vs. NHE (pH = 7) and is sufficient for water reduction to hydrogen. Whereas its VB top locates at about 1.4 V, resulting in a small thermodynamic driving force for water or organic pollutants oxidation [9]. In this regard, modulating the electronic structure of g-C$_3$N$_4$ by decreasing the VB position to enhance photooxidation is highly desirable. Furthermore, the photocatalytic efficiency of bulk g-C$_3$N$_4$ is limited due to fast recombination of photogenerated electron–hole pairs. To resolve this problem, many methods have been proposed including protonation [10], doping (boron [11], fluorine [12], and sulfur [13,14]), optimizing porous structure [15–18], and coupling g-C$_3$N$_4$ with metals [19,20]. In particular, there is a great interest in combining g-C$_3$N$_4$ with carbon-based materials to improve conductivity and catalytic performance [21]. Fullerenes (C$_{60}$) is suitable for efficient electron transfer because of the minimal changes of structure and salvation associated with electron transfer [22–25]. C$_{60}$/photocatalysts have been prepared to improve the performance of photocatalyst [26–28]. However, the mineralization and ring opening ability of g-C$_3$N$_4$ for benzene-based series is low, due to high VB position. To improve the deep photooxidation ability of g-C$_3$N$_4$, C$_{60}$/g-C$_3$N$_4$ composites may be ideal for enhancing charge separation efficiency and accelerating photoinduced electron transfer from g-C$_3$N$_4$ to reaction system. Such approach mainly relies on the excellent properties of C$_{60}$ molecules in terms of high exciton mobility (>1.3 cm^2 V^{-1} S^{-1}) and large exciton diffusion length [29].

Here C$_{60}$/g-C$_3$N$_4$ composite photocatalysts were utilized to degrade MB and phenol under visible light irradiation ($\lambda > 420$ nm). By incorporating electron-acceptor, C$_{60}$ monomer, into g-C$_3$N$_4$

* Corresponding author. Tel.: +86 10 62787601; fax: +86 10 62787601.
E-mail address: zhuyf@tsinghua.edu.cn (Y. Zhu).

matrix, the VB of g-C_3N_4 shifted to lower energy position. The deep photooxidation activities for phenol and MB of C_{60}/g-C_3N_4 are about 2.9 and 3.2 times as high as those of bulk g-C_3N_4. It was also found that the organic pollutants can be directly oxidized by holes and •OH in the presence of C_{60}/g-C_3N_4 photocatalyst.

2. Experimental

2.1. Materials

High-purity (99.9%) C_{60} powder was supported by J&K Scientific Ltd. Dicyandiamide (label as "DCDA") and urea was purchased from Sinopharm Chemical Reagent Corp, P. R. China. All other reagents used in this research were analytically pure and used without further purification. g-C_3N_4 powders was synthesized as described previously [30]. Dicyandiamide (3 g) (Aldrich, 99%) in an open crucible was heated in air with a ramping rate of 2.3 °C min^{-1} until the temperature reach 550 °C, and then was held at 550 °C for 4 h. The product was collected and ground into powder in an agate mortar for further characterization and performance measurements. It should be claimed that the widely used "g-$C_3N_{4''}$" in the literature is actually nonstoichiometric. Here we use "g-C_3N_4''" to describe the products just to keep consistent with the general usage.

2.2. Synthesis of C_{60}/g-C_3N_4 samples

The typical C_{60}/g-C_3N_4 composite were prepared as follows. C_{60} and dicyandiamide mixture was ball-milled (300 rps) for 30 min, resulting in ultrafine light-purple powder. Then, the light-purple powder was put in a muffle furnace and heated in static air to 550 °C with a ramping rate of 2.3 °C min^{-1}, and then was held at 550 °C for 4 h. The product was collected and ground into powder in an agate mortar for further characterization and performance measurements. With different amount addition of C_{60}, the colors of the final products are different. The C_{60}/g-C_3N_4 photocatalysts with different C_{60}/DCDA mass ratio, from 0.02 wt% to 1.0 wt%, were prepared according to above method. The C_{60}/g-C_3N_4 composites were marked as CCN-X. X indicates C_{60}/DCDA mass ratio in preparation, which are 0, 0.02, 0.03, 0.05, 0.06, 0.10, 0.27, 0.50 and 1.00, respectively.

The electrodes were prepared as follows. 4 mg of as-prepared photocatalyst was suspended in 2 mL water to produce slurry, which was then dip-coated onto a 2 cm × 4 cm indium-tin oxide (ITO) glass electrode. Electrodes were exposed to UV light for 10 h to eliminate ethanol and subsequently calcined at 200 °C for 8 h under N_2 flow (rate = 60 mL min^{-1}). All investigated electrodes were of similar thickness (0.8–1.0 μm).

2.3. Characterizations

Transmission electron microscopy (TEM) images were obtained by JEOL JEM-2011F field emission transmission electron microscope with an accelerating voltage of 200 kV. To avoid electron beam-induced damage, low-intensity beam was used for collecting selected area electron diffraction (SAED) patterns. X-ray diffraction (XRD) patterns of the powders were recorded at room temperature by a Bruker D8 Advance X-ray diffractometer. The diffuse reflectance absorption spectra (DRS) of the samples were recorded in the range from 250 to 800 nm using a Hitachi U-3010 spectroscope equipped with an integrated sphere attachment and $BaSO_4$ was used as a reference. Raman spectra were recorded on a microscopic confocal Raman spectrometer (Renishaw 1000 NR) with an excitation of 514.5 nm laser light. The room-temperature photoluminescence (PL) spectra of g-C_3N_4 and C_{60}/g-C_3N_4 samples were

investigated utilizing the Perkin-Elmer LS55 spectrophotometer equipped with xenon (Xe) lamp with an excitation wavelength of 370 nm. Fourier transform infrared (FTIR) spectra were carried out using Perkin-Elmer spectrometer in the frequency range of 4000–450 cm^{-1} with a resolution of 4 cm^{-1}. X-ray photoelectron spectroscopy (XPS) was measured in a PHI 5300 ESCA system. The beam voltage was 3.0 kV, and the energy of Ar ion beam was 1.0 keV. The binding energies were normalized to the signal for adventitious carbon at 284.8 eV. The Brunauer–Emmett–Teller (BET) surface area measurements were performed by a micromeritics (ASAP 2010 V5.02H) surface area analyzer. The nitrogen adsorption and desorption isotherms were measured at 77 K after degassing the samples on a Sorptomatic 1900 Carlo Erba Instrument. The electron spin resonance (ESR) signals of radicals spin-trapped by spin-trap reagent 5,5′-dimethyl-1-pirroline-*N*-oxide (DMPO) (purchased from Sigma Chemical Co.) were examined on a Bruker model ESR JES-FA200 spectrometer equipped with a quanta-Ray Nd:YAG laser system as the irradiation source (λ = 420 nm). To minimize experimental errors, the same type of quartz capillary tube was used for all ESR measurements. The ESR spectrometer was coupled to a computer for data acquisition and instrument control. Magnetic parameters of the radicals detected were obtained from direct measurements of magnetic field and microwave frequency. Electrochemical and photoelectrochemical measurements were performed in a three electrode quartz cells with 0.1 M Na_2SO_4 electrolyte solution. Platinum wire was used as counter and saturated calomel electrode (SCE) used as reference electrodes, respectively. g-C_3N_4 and C_{60}/g-C_3N_4 film electrodes on ITO served as the working electrode. The photoelectrochemical experiment results were recorded with an electrochemical system (CHI-660B, China). The visible irradiation was obtained from a 500 W Xe lamp (Institute for Electric Light Sources, Beijing) with a 420 nm cut-off filter. Potentials are given with reference to the SCE. The photoresponses of the photocatalysts as visible light on and off were measured at 0.0 V. Electrochemical impedance spectra (EIS) were measured at 0.0 V. A sinusoidal ac perturbation of 5 mV was applied to the electrode over the frequency range of 0.05–10^5 Hz. The temperature programmed deoxidizing (TPD) measurement using helium (He) gas was performed in a specially designed quartz tube with 0.03 g of C_{60}/g-C_3N_4 sample. The tube was put in a cylindrical electric furnace. Temperature of the furnace was controlled by a programmable regulator with the thermocouple. A thermal conductivity detector (TCD) was used to detect He consumption during the vacuum treatment process. The g-C_3N_4 and C_{60}/g-C_3N_4 samples were pretreated by nitrogen gas from room temperature to 120 °C at a temperature ramping rate of 5 °C min^{-1} for 2 h. Then it cooled naturally to the room temperature in N_2 atmosphere. Afterwards, Ar + O_2 mixture gas was introduced into the homemade quartz tube equipped with g-C_3N_4 and C_{60}/g-C_3N_4 samples to reach saturation of adsorption capacity, and then changed to He and the gas flow rate was set at 25 mL min^{-1} accompanying with the temperature gradually increased to 500 °C to detect oxygen desorption.

2.4. Photocatalytic experiments

The photocatalytic activities were evaluated by the decomposition of methylene blue (MB) and phenol under visible light irradiation (λ > 420 nm). Visible irradiation was obtained from a 500 W Xe lamp (Institute for Electric Light Sources, Beijing) with a 420 nm cut off filter, and the average visible light intensity was 38 mW cm^{-2}. 25 mg of photocatalyst was totally dispersed in an aqueous solution of MB (50 mL, 0.01 mM) or phenol (50 mL, 5 ppm). Before irradiation, the suspensions were magnetically stirred in dark for 60 min to get absorption-desorption equilibrium between the photocatalyst and MB (phenol). At certain time intervals,
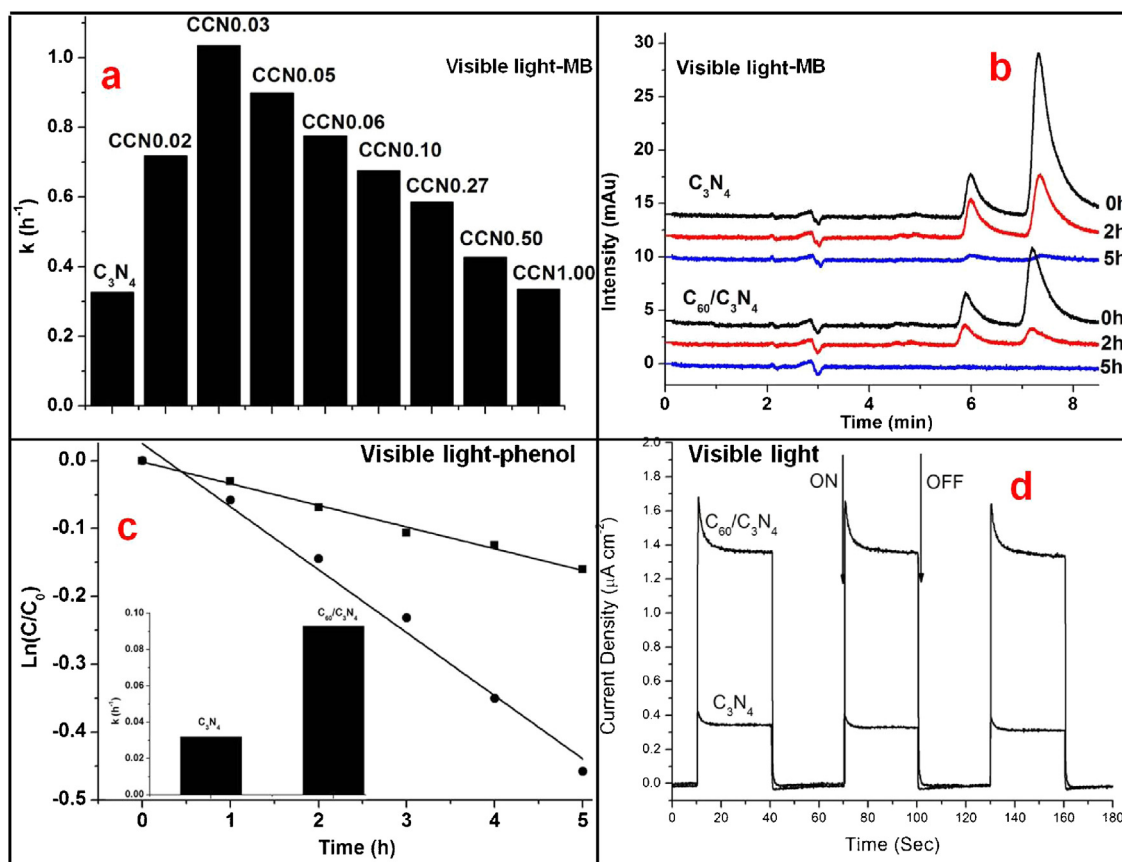
Fig. 1. (a) Apparent rate constants for MB photocatalytic degradation; (b) HPLC results at different irradiation intervals during MB photocatalytic degradation; (c) Apparent rate constants for the photocatalytic degradation of phenol; (d) Photoresponses intensity of film electrodes in Na_2SO_4 solution, over g-C_3N_4 and C_{60}/g-C_3N_4 photocatalysts under the visible light irradiation ($\lambda > 420$ nm, [MB] = 0.01 mM, [phenol] = 5 ppm, [Na_2SO_4] = 0.1 M).

3 mL aliquots were sampled and centrifuged to remove the particles. The concentration of MB was analyzed by recording the absorbance at the characteristic band of 663 nm using a Hitachi U-3010 UV–Vis spectrophotometer and phenol was detected using a HPLC method with a UV detector at 270 nm. To investigate the active species generated in the photocatalytic degradation process, the experiments of free radicals (hydroxyl radical (•OH) and hole (h^+) capture were carried out by *tert*-butylalcohol (*t*BuOH) and ethylenediamine tetraacetic acid disodium salt (EDTA-2Na), respectively.

3. Results and discussion

3.1. Photocatalytic activity and photocurrent response

Fig. 1a and b shows the photocatalytic activity of g-C_3N_4 and C_{60}/g-C_3N_4 samples for MB photodegradation under visible light irradiation, respectively. Significant differences in the catalytic behaviors were observed, and the photodegradation process is fit to pseudo-first-order kinetics, in which the value of rate constant k is equal to the corresponding slope of the fitting line. All the C_{60}/g-C_3N_4 samples exhibit higher photocatalytic activities than bulk g-C_3N_4. CCN-0.03 shows the highest activity, which is 3.2 times as high as that of g-C_3N_4. Results show that C_{60} loading amount has a great influence on the photocatalytic activity of C_{60}/g-C_3N_4 photocatalyst. As indicated in Fig. 1a, the apparent reaction rate constant k is 0.32617, 0.71887, 1.03648, 0.8994, 0.77661, 0.67621, 0.58483, 0.42796 and 0.33653 h^{-1}, respectively, for CCN-0, CCN-0.02, CCN-0.03, CCN-0.05, CCN-0.06, CCN-0.10, CCN-0.27, CCN-0.50, and CCN-1.00. When C_{60} loading amount is

below 0.03%, the photocatalytic activities increased with the increase of loading amount. However, when the loading amount exceeds 0.03%, the photocatalytic activities of C_{60}/g-C_3N_4 composites decreased as the amount of C_{60} increased. The optimal loading amount of C_{60} on g-C_3N_4 is 0.03% according to photocatalytic activity. In the following text, C_{60}/g-C_3N_4 composite refers to this optimal sample. This result implies that the interaction between C_{60} and g-C_3N_4 photocatalyst take an important role in the enhancement of photoactivity [28]. As shown in Fig. 1b, the photodecomposition process of MB under visible-light irradiation is demonstrated by HPLC. The typical HPLC chromatograms in the presence of g-C_3N_4 and C_{60}/g-C_3N_4 are recorded by UV–visible detector. After 2 h, the concentration of MB in C_{60}/g-C_3N_4 system is much lower than that in g-C_3N_4 system. The evidence further proves that the oxidation rate of C_{60}/g-C_3N_4 was faster. At the same time, no new intermediates or products forms, indicating the photocatalytic decomposition process for pollutants is similar with g-C_3N_4 even after being modified by C_{60}. The photocatalytic decomposition of phenol by C_{60}/g-C_3N_4 and g-C_3N_4 photocatalyst under visible light irradiation is also carried out (Fig. 1c). The C_{60}/g-C_3N_4 sample showed much higher photocatalytic activity for the decomposition of phenol than g-C_3N_4. The apparent reaction rate constant k is 0.0929 and 0.0319 h^{-1} for C_{60}/g-C_3N_4 and g-C_3N_4 samples, respectively. Therefore, it is an efficient way to enhance the photocatalytic activity of g-C_3N_4 by modifying with C_{60}.

The photocurrent responses of C_{60}/g-C_3N_4 and g-C_3N_4 after deposition on ITO electrodes under visible light ($\lambda > 420$ nm), are shown in Fig. 1d. The photocurrent intensity remains at a constant value when the light is on and rapidly decreases to zero as long as the light is turned off. It is obvious to observe that the
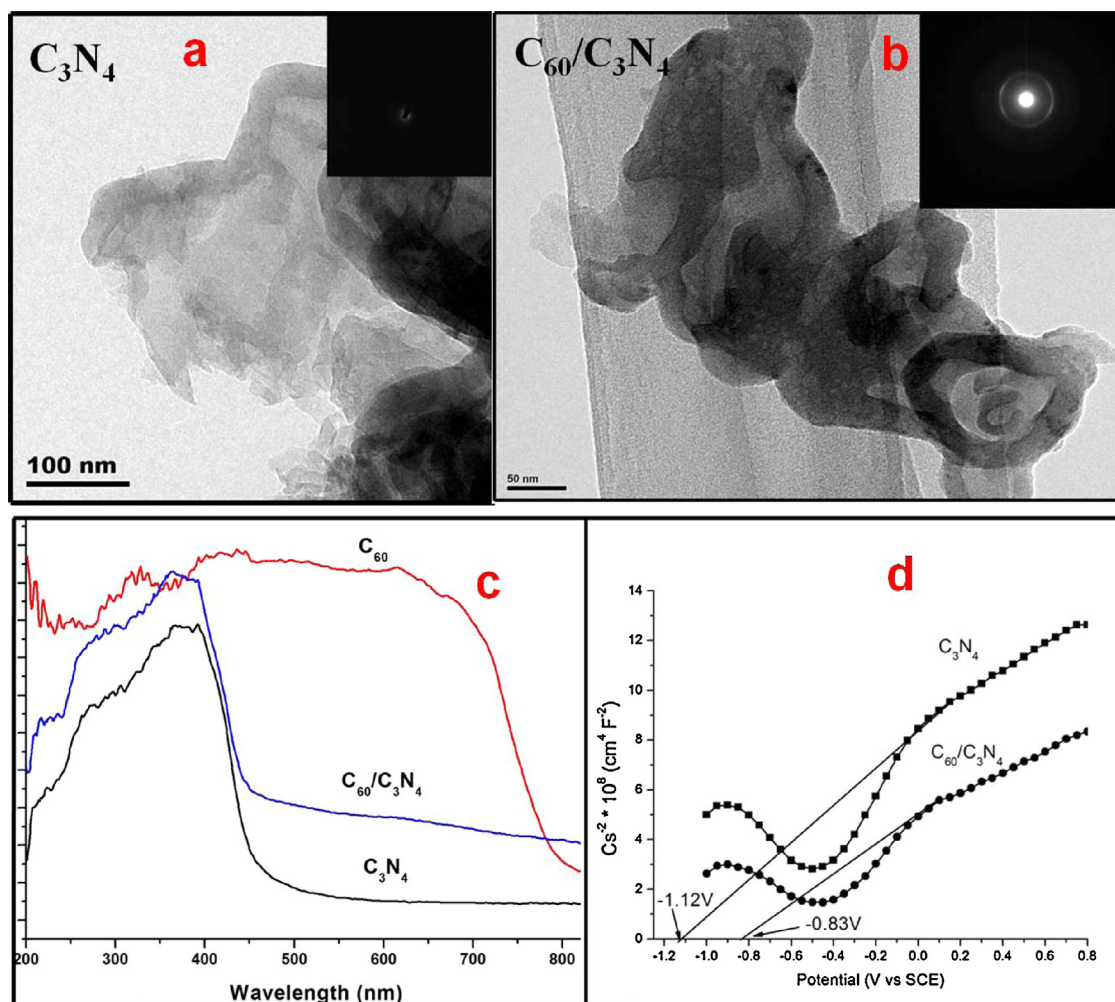
Fig. 2. (a) TEM and SAED (insert) images of g-C_3N_4 photocatalyst; (b) TEM and SAED (insert) images of C_{60}/g-C_3N_4 photocatalyst; (c) Diffuse reflectance absorption spectra of C_{60}, g-C_3N_4 and C_{60}/g-C_3N_4 photocatalysts; (d) Mott–Schottky (MS) plots of the different catalysts film electrodes. The MS plots were obtained at a frequency of 1 kHz in an aqueous solution of Na_2SO_4 (0.1 M).

photocurrent over C_{60}/g-C_3N_4 is greatly improved, which is about 4.0 times as high as that of bulk g-C_3N_4. Because the photocurrent is formed mainly by the diffusion of photogenerated electrons to the back contact and simultaneously holes are taken up by the hole acceptor in the electrolyte [31]. The enhanced photocurrent over C_{60}/g-C_3N_4 sample implies more efficient separation of the photoinduced electron–hole pairs and longer lifetime of the photogenerated charge carriers than that of bulk g-C_3N_4, which is beneficial for its enhanced photocatalytic activity.

3.2. Conjugated structure and optical properties

Fig. 2a and b shows the typical TEM and SAED (insert) images of g-C_3N_4 and C_{60}/g-C_3N_4 samples, which demonstrate similar morphology. Maybe C_{60} nanoparticles are so few in amount when compared with g-C_3N_4 nanosheets, and also were easy to be wrapped by g-C_3N_4 nanosheet, the C_{60} nanoparticles could hardly be seen in local TEM images. From the inset SAED in Fig. 2a and b, it can be observed that C_{60}/g-C_3N_4 presents higher crystallinity than bulk g-C_3N_4, and this may be beneficial for enhancing photocatalytic activity. These observations demonstrate that C_{60} nanoparticles are well dispersed and attached on g-C_3N_4 nanosheets.

The absorption range of light plays an important role in the photocatalysis, especially for the visible light photodegradation of

contaminants. As shown in Fig. 2c, which shows the UV–vis diffuse reflectance spectroscopy (DRS) of bulk g-C_3N_4 and C_{60}/g-C_3N_4, there is about red shift of *ca.* 20 nm in the absorption edge and enhanced absorption intensity of C_{60}/g-C_3N_4 samples, which could be responsible for the visible-light induced photocatalytic activity. The value of band gap for g-C_3N_4 and C_{60}/g-C_3N_4 are determined as 2.70 and 2.58 eV by extrapolation method, respectively. Moreover, the strong absorption of C_{60} in visible region (400–800 nm) is responsible for narrowing of band gap. In order to better understand the differences in the photoelectric properties of g-C_3N_4 and C_{60}/g-C_3N_4, their electrode are examined under various electrochemical conditions. Fig. 2d shows Mott–Schottky (MS) plots, $1/C^2$ versus E, for the g-C_3N_4 and C_{60}/g-C_3N_4. Reversed sigmoidal plots are observed with an overall shape that is consistent with that of typical n-type semiconductors [32]. The intersection point of the potential and linear potential curves give a flat band potential, which in this case is approximately −1.12 V and −0.83 V versus Ag/AgCl for g-C_3N_4 and C_{60}/g-C_3N_4, respectively. The C_{60}/g-C_3N_4 experiences a positive shift of the flat-band potential when compared with g-C_3N_4. According to the value of band gap (DRS result), the estimated positions of valence band maximum (VBM) are 1.58 and 1.75 V versus Ag/AgCl for g-C_3N_4 and C_{60}/g-C_3N_4, respectively. The VBM of C_{60}/g-C_3N_4 is lowered than that of g-C_3N_4 by 0.17 V. The lowering of the VBM indicates that C_{60}/g-C_3N_4 has stronger oxidation ability theoretically. Furthermore, it was noteworthy that
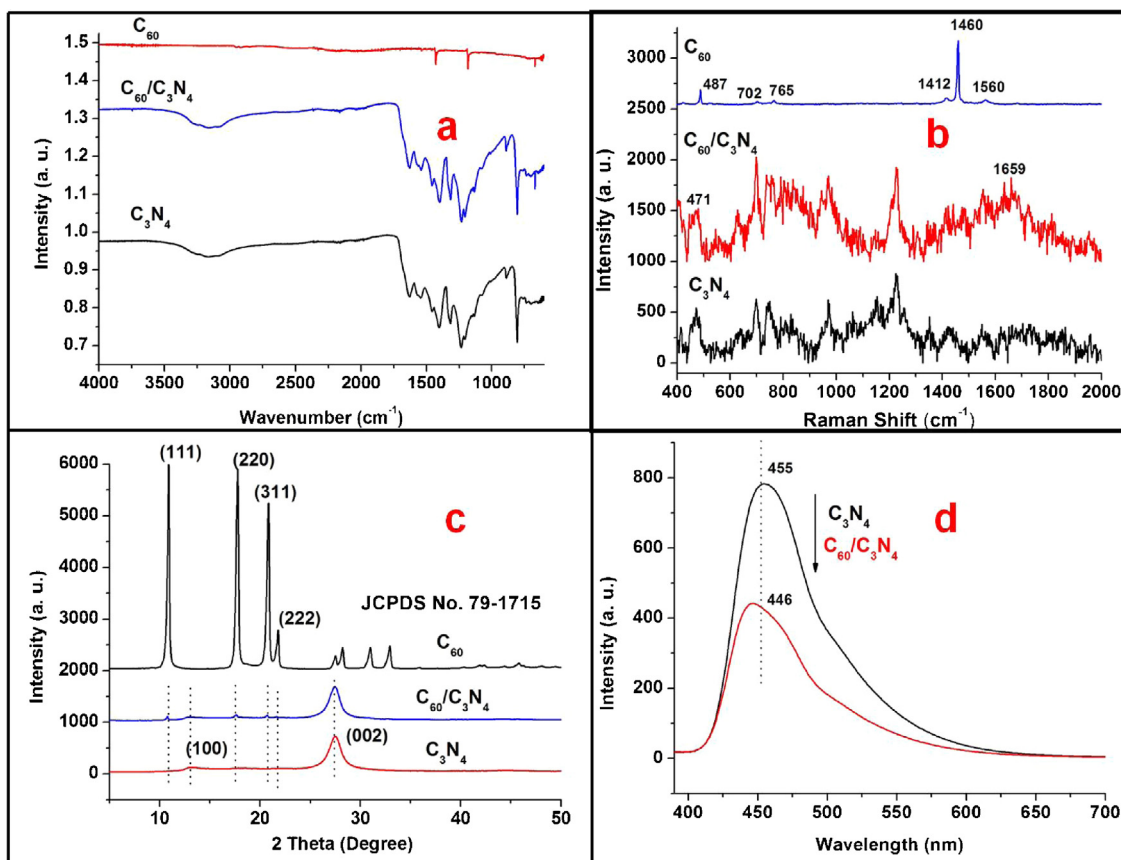
Fig. 3. (a) FTIR spectra of g-C_3N_4 and C_{60}/g-C_3N_4 photocatalysts; (b) Raman spectra of g-C_3N_4 and C_{60}/g-C_3N_4 photocatalysts; (c) XRD patterns of g-C_3N_4 and C_{60}/g-C_3N_4 photocatalysts; (d) Room-temperature PL excitation and emission spectra of g-C_3N_4 and C_{60}/g-C_3N_4 photocatalysts (λ_{ex} = 370 nm).

the slope of the linear region for C_{60}/g-C_3N_4 electrode is lower in value, which suggests a higher donor density. According to photocatalytic mechanism, the higher donor density for the doped electrode, the photocatalytic degradation rate is faster [33]. This has been proved that the photocurrent of C_{60}/g-C_3N_4 sample is larger than g-C_3N_4 sample. Therefore, the enhancement of photocatalytic activity could be attributed to the higher separation efficiency of electron–hole pairs, and a large number of holes participated in the photocatalytic process caused by C_{60}.

In order to get an insight into the nature of the interface interaction in C_{60}/g-C_3N_4 sample, FTIR and Raman spectra are conducted. Fig. 3a shows a comparison of the FTIR spectra of C_{60}, g-C_3N_4 and C_{60}/g-C_3N_4 samples. In the case of g-C_3N_4, the broad band at 3155 cm^{-1} is attributed to stretching modes of NH and NH$_2$. The band at 1313 cm^{-1} corresponds to C(sp^2)–N stretching, and the band at 1635 cm^{-1} assigns to C(sp^2)=N stretching modes. The 807 cm^{-1} band is attributed to s-triazine ring vibration modes. The C–NH–C unit is found in melem (1235 and 1319 cm^{-1}) [34]. The FTIR spectrum of pure C_{60} consists of three absorbance bands at 669, 1182, and 1429 cm^{-1} [35]. A sharp absorption peaks at 669 cm^{-1} for C_{60} is observed in C_{60}/C_3N_4 sample. Other peaks at 3155, 1635, 1319, 1313, 1235, 807 cm^{-1} may be attributed to characteristic vibrational of g-C_3N_4 in composite sample. However, for C_{60}/g-C_3N_4, 1182, and 1429 cm^{-1} band cannot be observed, indicating that the two bands are submerged beneath the strong g-C_3N_4 bands. Raman spectroscopy is widely used to study the vibrational properties of carbon related materials. Raman scattering spectra of pristine C_{60}, g-C_3N_4 and C_{60}/g-C_3N_4 samples are collected with the laser wavelength of 514 nm in order to minimize the effect of fluorescence effect (Fig. 3b). The vibration frequencies of H$_g$(7), A$_g$(2), and H$_g$(8) modes for pristine C_{60} are 1412, 1460, and

1560 cm^{-1}, respectively, in agreement with the previous report [36]. It is noteworthy that the A$_g$(2) peak located at 1460 cm^{-1} disappeared in spectra for C_{60}/g-C_3N_4 composite. It is known that fullerene compounds with charge transfer exhibit significant line shifts in their Raman spectra. One of the most sensitive modes to charge transfer in C_{60} is the A$_g$(2) mode [37]. Raman spectra of C_{60}/g-C_3N_4 sample shows obvious change of the A$_g$(2) mode and this can be considered as reliable evidence for charge transfer in the composites. The similar conclusions have been demonstrated, For example, in the relatively well studied charge-transfer complex TDAE-C_{60} this mode is downshifted 6 cm^{-1} while the A$_g$(1) mode is down-shifted only 2 cm^{-1} and the H$_g$(1) mode remains unshifted [38]. Alkali metal fullerides show a downshift of the A$_g$(2) mode by 6 cm^{-1} per each dopant metal atom [39]. Several characteristic peaks of g-C_3N_4 at 458, 693, 734, 964, 1217, and 1296 cm^{-1} are observed. There are two peaks observed at 1347 cm^{-1} (D band) and 1569 cm^{-1} (G band). The G band corresponds to the symmetric E_{2g} vibrational mode in graphite-like structures and is attributed to graphite-like sp^2 microdomains in the products, while the D band corresponds to disordered sp^2 microdomains introduced by the linking with N atoms [40]. In the case of C_{60}/g-C_3N_4, the peak of G band is broadened and the center of the peak shifts to a higher frequency from 1569 to 1659 cm^{-1}. It is evidence of the presence of the electron transfer from g-C_3N_4 to C_{60}, namely, a strong interface interaction. Compared with pristine C_{60}, the spectrum of the C_{60}/g-C_3N_4 changes considerably. The peak of Ag(2) mode is observed and broadened in C_{60}/g-C_3N_4, this proves the presence of the strong interface interaction between g-C_3N_4 and C_{60}.

XRD pattern is used to investigate the phase structures of the samples, and the typical diffraction patterns are shown in Fig. 3c. The peaks at 13.1° and 27.4° in the XRD patterns of the samples

could be indexed to the hexagonal phase of g-C$_3$N$_4$ (JCPDS 087-1526). The peak at 27.4° is due to the stacking of the conjugated aromatic system, which is indexed for graphitic materials as the (0 0 2) peak of the g-C$_3$N$_4$. The small angle peak at 13.08°, corresponding to interplanar distance of 0.676 nm, is indexed as (1 0 0), which is associated with interlayer stacking [30]. The intensity of the peak is decreased which indicated that C$_{60}$ nanoparticles may be wrapped in the interlayer of g-C$_3$N$_4$ nanoplates and weaken the force of interlayer stacking, accordingly. The crystalline peaks of C$_{60}$ located at (1 1 1), (2 2 0), (3 1 1), (2 2 2) (JCPDS. No. 79-1715) are also detected in C$_{60}$/g-C$_3$N$_4$ sample, which enhances the crystalline property and is beneficial for its enhanced photocatalytic activity. Carbon nitride (g-C$_3$N$_4$) network materials have been produced as disordered structures by precursor-based methods, which may contains two main isomers: triazine (C$_3$N$_3$) and heptazine (C$_6$N$_7$) units, not an ideal structure. And the proportion of them strongly depends on the precursors and condensation process during synthesis. Therefore, in the process of calcinations for C$_{60}$ and g-C$_3$N$_4$, it is likely to cleave –NH– between C$_3$N$_3$ and C$_6$N$_7$ by C$_{60}$ clusters and connect with g-C$_3$N$_4$ by chemical bond C–N. To further investigate the chemical interaction between g-C$_3$N$_4$ and C$_{60}$/g-C$_3$N$_4$, the XPS and FTIR results could provide solid evidence to demonstrate the chemical interaction. As shown in Fig. S1a, the C2 peak centered at 288.2 eV is the main contribution in their C1s spectra, which originated from sp^2 C atoms bonded to N inside the aromatic structure, whereas the C1 peak at 288.5 eV is assigned to sp^2 C atoms in the aromatic ring attached to the –NH–/–NH$_2$ group [41]. The lowest energy contribution C3 at 284.8 eV is typically assigned to surface contamination carbon. After C$_{60}$ modification, the intensity of C1 peak reduces obviously, indicating the –NH–/–NH$_2$ group decrease due to the chemical bond C–N between C$_{60}$ and g-C$_3$N$_4$. In Fig. S1b, the high resolution N1s spectra can be also deconvoluted into three different peaks at binding energies of ≈400.2 (N1), 398.5 (N2) and 404.2 eV (N3), respectively. The absence of a peak above 401.0 eV reveals that the samples do not possess the N–N bonding configuration. The dominant N1 is commonly attributed to sp^2 N atoms involved in triazine rings, while the medium N2 is assigned to bridging N atoms in N–(C)3 or N bonded with H atoms. The very weak N3 can be assigned to the charging effects or positive charge localization in heterocycles and the cyano-group [41]. The weak N3 peak for C$_{60}$/g-C$_3$N$_4$ composite becomes clearer with respect to that of bulk g-C$_3$N$_4$, indicating more positive charge is introduce by carbon, which is connected with nitrogen (C–N) during the calcination process. Furthermore, the O1s peak located at 532.3 eV was attributed to surface hydroxyl group, which is

reduced after C$_{60}$ modification in composite system compared with bulk g-C$_3$N$_4$ (Fig. S1c), suggesting more carbon from C$_{60}$ could be introduced and then decreased the number of oxygen. These assignments are in good agreement with C1s and N1s results for the two systems. For further figuring out the chemical interaction of C$_{60}$ species incorporated in g-C$_3$N$_4$ system, FTIR result (Fig. S1d) shows a typical IR peaks located at 672 cm^{-1} of C$_{60}$ could be well defined, indicating C$_{60}$ can be trapped by the g-C$_3$N$_4$ nanoplates via the calcination route. We also investigated whether C$_{60}$ can leach from the C$_{60}$/g-C$_3$N$_4$ composite system in toluene solution. As shown in Fig. S2, no color change can be observed to the case of the C$_{60}$/g-C$_3$N$_4$ composites in toluene at room temperature for 2 h. The result clearly shows that the loaded C$_{60}$ clusters in the g-C$_3$N$_4$ system nearly cannot be extracted by toluene solvent, suggesting an intense chemical interaction formed between C$_{60}$ clusters and g-C$_3$N$_4$.

In the previous studies, photoluminescence (PL) analysis is used to reveal the efficiency of charge carrier trapping, transfer, and separation and to investigate the fate of photogenerated electrons and holes in semiconductors, because the PL emission results from the recombination of free charge carriers [21]. Herein, we present the suitable PL measurement for g-C$_3$N$_4$ and C$_{60}$/g-C$_3$N$_4$, as shown in Fig. 3d. Obviously, in comparison with bulk C$_3$N$_4$, the intensity of the PL signal for the C$_{60}$/g-C$_3$N$_4$ composite is much lower and shows an obvious blue-shift. This indicates that the composite has a lower recombination rate of electrons and holes under visible-light irradiation, which is mainly due to the fact that the electrons are excited from the valence band to the conduction band and then transfer to C$_{60}$ nanoparticles, preventing a direct recombination of electrons and holes. This may be ascribed to C$_{60}$, which becoming the separation center of the photogenerated electrons and holes. Because these particles are considered to be a good electron-acceptor material to effectively hinder the electron–hole pair recombination due to its two-dimensional π-conjugation structure.

Temperature-programmed desorption (TPD) measurements have been widely utilized to estimate the amount of adsorbates and the strength of adsorption on surfaces. To utilize the O$_2$-TPD experiments, we can expect to obtain useful information regarding the adsorption sites of oxygen on the surface of photocatalysts and useful knowledge for improving photocatalytic performance [42]. TPD spectra of O$_2$ from g-C$_3$N$_4$ and C$_{60}$/g-C$_3$N$_4$ samples are shown in Fig. 4a. Corresponding to the trend in photocatalytic activity, the desorption peak of O$_2$ from the C$_{60}$/g-C$_3$N$_4$ surface was the more intense, indicating that C$_{60}$/g-C$_3$N$_4$ can adsorb the more amount of O$_2$ than bulk g-C$_3$N$_4$. The amount and strength of

Fig. 4. (a) O$_2$-TPD spectra of g-C$_3$N$_4$ and C$_{60}$/g-C$_3$N$_4$ photocatalysts. Oxygen was adsorbed at room temperature, and the heating rate was 5 °C min^{-1}; (b) N$_2$ adsorption–desorption isotherms and Barret–Joyner–Halenda (BJH) (inset) pore size distribution plots of g-C$_3$N$_4$ and C$_{60}$/g-C$_3$N$_4$ photocatalysts.

molecular O_2 would strongly affect photocatalytic activity. Higher adsorption amounts and stronger adsorption are very important for achieving a high photocatalytic activity. The specific surface area is demonstrated by the N_2 adsorption/desorption analysis (Fig. 4b) and calculated by the Brunauer–Emmett–Teller (BET) model. The specific surface area of C_{60}/g-C_3N_4 is 12.1 m^2/g, which is higher than 8.5 m^2/g for bulk C_3N_4, indicating that there may be more adsorption sites for O_2 molecule, which is consistant with O_2-TPD results. The pore width of C_{60}/g-C_3N_4 is about 15 nm, while is about 17 nm for g-C_3N_4. The slight decrease of pore width may be ascribed to C_{60} occupying the stacking interlayer structure of the g-C_3N_4 nanoplates.

3.3. Proposed mechanism

ESR technique and trapping experiments of radicals are performed to monitor the reactive oxygen species generated during the irradiation of as-prepared system. ESR results are shown in Fig. S3. Under visible light irradiation, same hydroxyl radical and much superoxide radical for C_{60}/g-C_3N_4 than g-C_3N_4 samples in H_2O and DMSO are all observed, respectively. To further reveal the photocatalytic mechanism, the main oxidative species in the photocatalytic process are detected through the trapping experiments of radicals using t-BuOH as hydroxyl radical scavenger [43] and EDTA-2Na as holes radical scavenger [44]. As shown in Fig. 5a and b the photocatalytic activity of g-C_3N_4 decreases slightly by the addition of hydroxyl radical scavenger and hole capture, while the photocatalytic activity of C_{60}/g-C_3N_4 samples reduced largely accordingly, indicating that hydroxyl radical and holes are the main oxidative species for C_{60}/g-C_3N_4 samples. In addition, N_2 is also a

good detective molecular to make certain the effect of O_2, shown in Fig. 5c and d. Under the anoxic suspension, the photodegraded rate of MB in g-C_3N_4 system is largely prohibited while it is slightly influenced in C_{60}/g-C_3N_4 system, indicating O_2 is even more important in the photodegradation process in g-C_3N_4 system that produces more superoxide radicals ($\bullet^-O_2$) than in C_{60}/g-C_3N_4 system. Base on the above analysis, it can be concluded that the photooxidation mechanism occurring on the surface of C_{60}/g-C_3N_4 may involve the direct reaction of the organic chemical (dye) with strong oxidizing hydroxyl radical and holes. The main oxidative species in C_{60}/g-C_3N_4 system is not same as that of in g-C_3N_4 system which may be attributed to the superoxide radicals ($\bullet^-O_2$). These results indicate that the photocatalytic degradation mechanism of C_{60}/g-C_3N_4 on MB has been changed, compared with that of bulk g-C_3N_4 photocatalyst.

As discussed above, there may exist more active species (holes) in C_{60}/g-C_3N_4 system compared with bulk g-C_3N_4 system. Thus, it can be supposed that C_{60} could hinder the recombination of electrons–holes and accelerate the rate of charge transfer. Electrochemical impedance spectroscopy (EIS) Nyquist plot of bulk g-C_3N_4 and C_{60}/g-C_3N_4 samples is carried out to investigate the process of electron transfer. Considering that the preparation of the electrodes and electrolyte used are identical, the high frequency semicircle is relevant to the resistance of the electrodes. In electrochemical spectra, the high frequency arc corresponds to the charge transfer limiting process and can be attributed to the double-layer capacitance (C_{dl}) in parallel with the charge transfer resistance (R_{ct}) at the contact interface between the electrode and electrolyte solution [45]. As shown in Fig. 6, the arc radius on the EIS Nyquist plot of C_{60}/g-C_3N_4 composites is smaller than that of bulk g-C_3N_4 in the
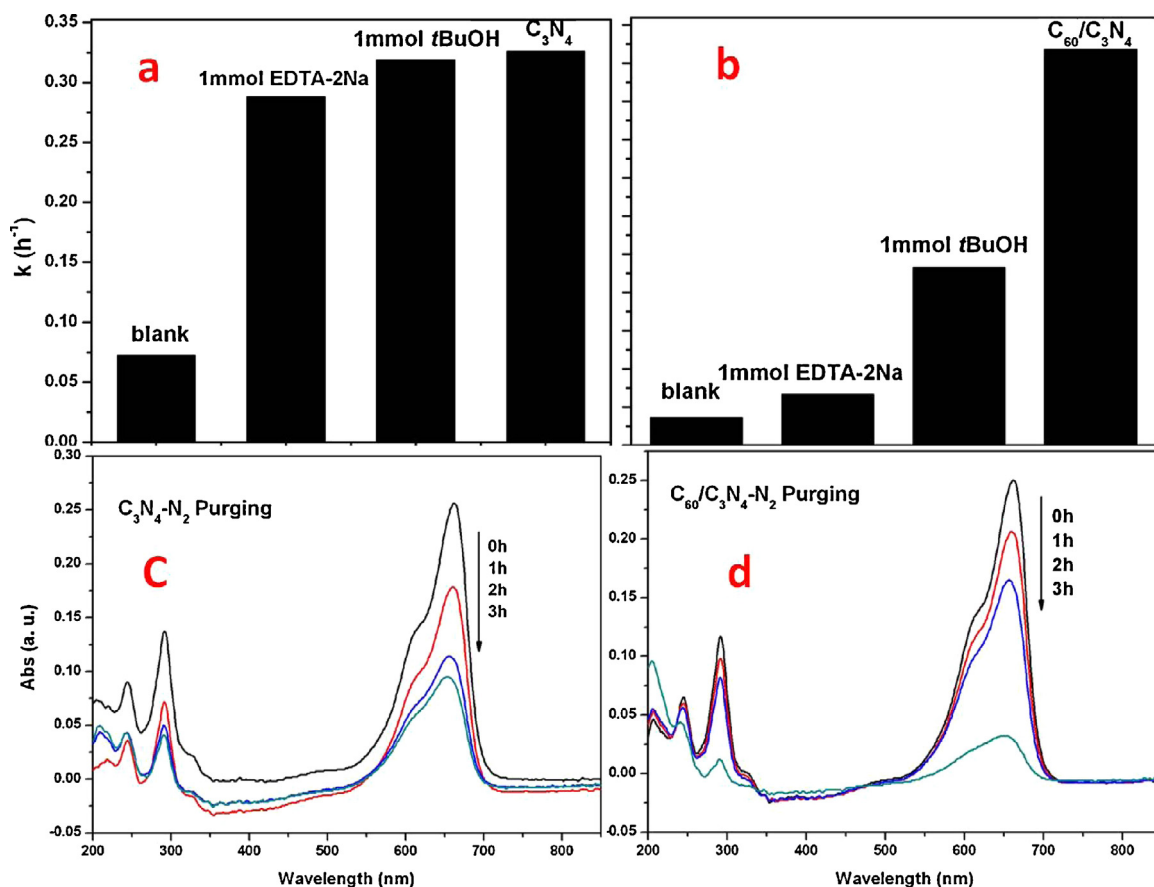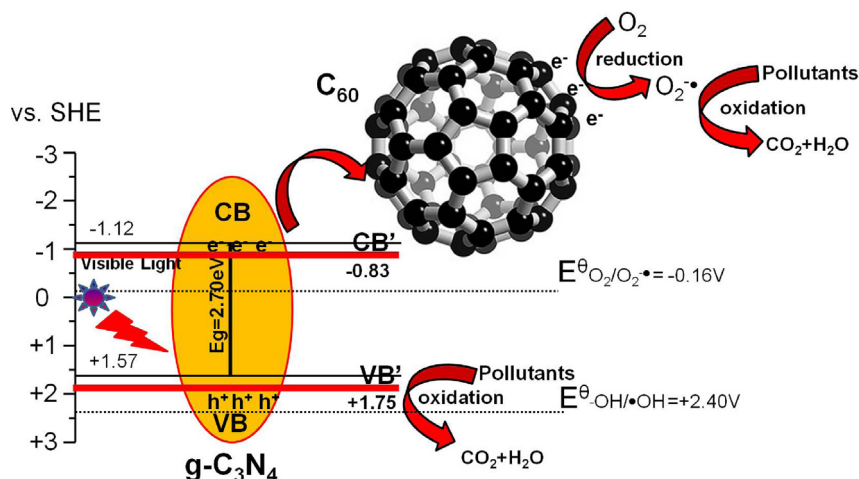

Fig. 5. (a and b) Apparent rate constants for MB photocatalytic degradation of over g-C_3N_4 and C_{60}/g-C_3N_4 photocatalysts with the addition of hole and radical scavenger under the irradiation of visible light ($\lambda > 420$ nm); (c and d) Plots of photogenerated superoxide radical trapping for MB photodegradation over g-C_3N_4 and C_{60}/g-C_3N_4 photocatalysts.

Scheme 1. Schematic drawing illustrating synthetic route and the mechanism of charge separation and photocatalytic process over g-C₃N₄ and C₆₀/g-C₃N₄ photocatalysts under visible light irradiation.

cases of both with and without light irradiation. This suggests that the former owns a more effective separation of photogenerated electron–hole pairs and faster interfacial charge transfer.

Based on the above results, a mechanism for separation and transportation of electron–hole pairs at the interface of C₆₀/g-C₃N₄ photocatalysts is proposed in Scheme 1. Under visible light irradiation, electrons (e⁻) are excited from the VB populated by N2p orbitals to the CB formed by C2p orbitals of g-C₃N₄, creating holes (h⁺) in the VB. Normally, these charge carriers quickly recombine and only a fraction of electrons could participate in the photocatalytic reaction. However, when g-C₃N₄ is connected with C₆₀ to form composites, these photogenerated electrons on the CB of g-C₃N₄ tend to transfer to C₆₀ particles due to their excellent electronic conductivity, leading to hole–electron separation. The transferred electrons will accumulate on the C₆₀ nanoparticles and presumably as interface bound exciton pairs to capture the adsorbed O₂ on g-C₃N₄ surface to form superoxide radical ($\bullet^-O_2$), and then participate in photocatalytic oxidation reaction. Meanwhile, on the VB of g-C₃N₄, the high separation efficiency of photoinduced electron–hole pairs is result in the increase of the number of holes, which could directly improve the moderate performance of mineralization ability and

ring opening for benzene series in degradation of organic pollutants.

4. Conclusions

In summary, C₆₀/g-C₃N₄ composites were synthesized using a facile routine thermal treatment process. After being modified by C₆₀, the photocatalytic activities and the photocurrent response of g-C₃N₄ on MB and phenol degradation under visible light irradiation increase to about 3.2, 2.9 and 4.0 times as high as those of bulk g-C₃N₄, respectively. The significant enhancement on photocatalytic performance was attributed to rapid photogenerated electron transfer rate and charge separation efficiency of C₆₀ in C₆₀/g-C₃N₄ composite. With the increased holes and •OH, which can directly participate in the photooxidation process in C₆₀/g-C₃N₄ system, C₆₀/g-C₃N₄ composites show improved mineralization and ring opening ability for benzene series. This work can provide important inspirations for developing of π-conjugated photocatalytic materials.

Acknowledgments

Appendix A. Supplementary data

Supplementary data associated with this article can be found, in the online version, at http://dx.doi.org/10.1016/j.apcatb.2014.01.046.

References

[1] G.S. Li, B. Jiang, X. Li, Z.C. Lian, S.N. Xiao, J. Zhu, D.Q. Zhang, H.X. Li, ACS Appl. Mater. Interfaces 5 (2013) 7190–7197.
[2] K. Vinodgopal, D.E. Wynkoop, P.V. Kamat, Environ. Sci. Technol. 30 (1996) 1660–1666.
[3] A. Ehret, L. Stuhl, M.T. Spitler, J. Phys. Chem. B 105 (2001) 9960–9965.
[4] I.K. Konstantinou, T.A. Albanis, Appl. Catal., B 49 (2004) 1–14.
[5] X.C. Wang, K. Maeda, A. Thomas, K. Takanabe, G. Xin, J.M. Carlsson, K. Domen, M. Antonietti, Nat. Mater. 8 (2009) 76–80.
[6] Y. Wang, X.C. Wang, M. Antonietti, Angew. Chem. Int. Ed. 51 (2012) 68–89.
[7] A. Thomas, A. Fischer, F. Goettmann, M. Antonietti, J.O. Muller, R. Schlogl, J.M. Carlsson, J. Mater. Chem. 18 (2008) 4893–4908.
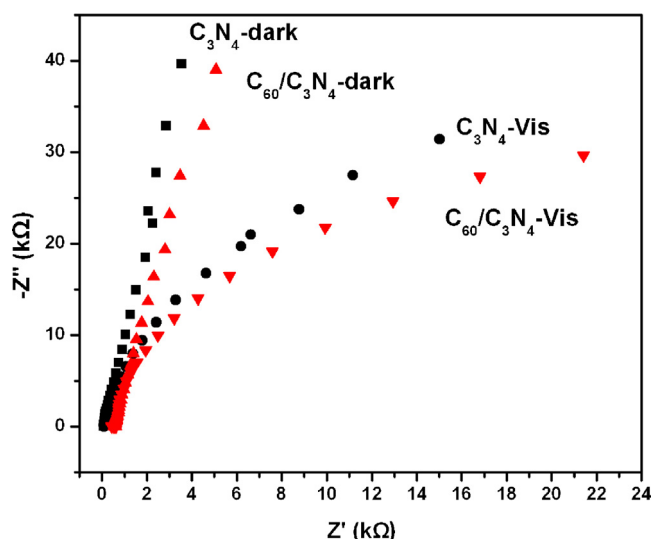

Fig. 6. EIS Nyquist plots of the g-C₃N₄ and C₆₀/g-C₃N₄ photocatalysts with light on/off cycles under the irradiation of visible light (λ > 420 nm). [Na₂SO₄ = 0.1 M].

[8] M. Antonietti, P. Fratzl, Macromol. Chem. Phys. 211 (2010) 166–170.
[9] Y.J. Cui, Z.X. Ding, P. Liu, M. Antonietti, X.Z. Fu, X.C. Wang, Phys. Chem. Chem. Phys. 14 (2012) 1455–1462.
[10] Y.J. Zhang, A. Thomas, M. Antonietti, X.C. Wang, J. Am. Chem. Soc. 131 (2009) 50–51.
[11] Y. Wang, H.R. Li, J. Yao, X.C. Wang, M. Antonietti, Chem. Sci. 2 (2011) 446–450.
[12] Y. Wang, Y. Di, M. Antonietti, H.R. Li, X.F. Chen, X.C. Wang, Chem. Mater. 22 (2010) 5119–5121.
[13] G. Liu, P. Niu, C.H. Sun, S.C. Smith, Z.G. Chen, G.Q. Lu, H.M. Cheng, J. Am. Chem. Soc. 132 (2010) 11642–11648.
[14] J.H. Zhang, J.H. Sun, K. Maeda, K. Domen, P. Liu, M. Antonietti, X.Z. Fu, X.C. Wang, Energy Environ. Sci. 4 (2011) 675–678.
[15] J.S. Zhang, X.F. Chen, K. Takanabe, K. Maeda, K. Domen, J.D. Epping, X.Z. Fu, M. Antonietti, X.C. Wang, Angew. Chem. Int. Ed. 49 (2010) 441–444.
[16] X.C. Wang, K. Maeda, X.F. Chen, K. Takanabe, K. Domen, Y.D. Hou, X.Z. Fu, M. Antonietti, J. Am. Chem. Soc. 131 (2009) 1680–1681.
[17] X.F. Chen, J.S. Zhang, X.Z. Fu, M. Antonietti, X.C. Wang, J. Am. Chem. Soc. 131 (2009) 11658–11659.
[18] Y. Guo, S. Chu, S.C. Yan, Y. Wang, Z.G. Zou, Chem. Commun. 46 (2010) 7325–7327.
[19] X.C. Wang, X.F. Chen, A. Thomas, X.Z. Fu, M. Antonietti, Adv. Mater. 21 (2009) 1609–1612.
[20] X.J. Bai, R.L. Zong, C.X. Li, D. Liu, Y.F. Liu, Y.F. Zhu, Appl. Catal., B 147 (2014) 82–91.
[21] Q.J. Xiang, J.G. Yu, M. Jaroniec, J. Phys. Chem. C 115 (2011) 7355–7363.
[22] T. Hasobe, S. Hattori, P.V. Kamat, S. Fukuzumi, Tetrahedron 62 (2006) 1937–1946.
[23] G. Yu, J. Gao, J.C. Hummelen, F. Wudl, A.J. Heeger, Science 270 (1995) 1789–1791.
[24] P.V. Kamat, M. Gevaert, K. Vinodgopal, J. Phys. Chem. B 101 (1997) 4422–4427.
[25] T. Hasobe, H. Imahori, S. Fukuzumi, P.V. Kamat, J. Phys. Chem. B 107 (2003) 12105–12112.
[26] H.B. Fu, T.G. Xu, S.B. Zhu, Y.F. Zhu, Environ. Sci. Technol. 42 (2008) 8064–8069.
[27] Y.Z. Long, Y. Lu, Y. Huang, Y.C. Peng, Y.J. Lu, S.Z. Kang, J. Mu, J. Phys. Chem. C 113 (2009) 13899–13905.
[28] S.B. Zhu, T.G. Xu, H.B. Fu, J.C. Zhao, Y.F. Zhu, Environ. Sci. Technol. 41 (2007) 6234–6239.
[29] J.F. Nierengarten, T. Gu, T. Aernouts, W. Geens, J. Poortmans, G. Hadziioannou, D. Tsamouras, Appl. Phys. A 79 (2004) 47–49.
[30] F. Goettmann, A. Fischer, M. Antonietti, A. Thomas, Angew. Chem. Int. Ed. 45 (2006) 4467–4471.
[31] N. Zhang, S.Q. Liu, X.Z. Fu, Y.J. Xu, J. Mater. Chem. 22 (2012) 5042–5052.
[32] G.L. Huang, R. Shi, Y.F. Zhu, J. Mol. Catal. A: Chem 348 (2011) 100–105.
[33] H. Maeda, K. Ikeda, K. Hashimoto, K. Ajito, M. Morita, A. Fujishima, J. Phys. Chem. B 103 (1999) 3213–3217.
[34] J.A. Singh, S.H. Overbury, N.J. Dudney, M.J. Li, G.M. Veith, ACS Catal. 2 (2012) 1138–1146.
[35] H.L. Huang, S.H. Goh, J.W. Zheng, D.M.Y. Lai, C.H.A. Huan, Langmuir 19 (2003) 5332–5335.
[36] D.S. Bethune, G. Meijer, W.C. Tang, H.J. Rosen, W.G. Golden, H. Seki, C.A. Brown, M.S. Devries, Chem. Phys. Lett. 179 (1991) 181–186.
[37] A. Talyzin, U. Jansson, J. Phys. Chem. B 104 (2000) 5064–5071.
[38] K. Pokhodnia, J. Demsar, A. Omerzu, D. Mihailovich, Phys. Rev. B: Condens. Matter 55 (1997) 3757–3762.
[39] M.S. Dresselhaus, G. Dresselhaus, P.C. Eklund, J. Raman Spectrosc. 27 (1996) 351–371.
[40] O. Akhavan, ACS Nano 4 (2010) 4174–4180.
[41] S.B. Yang, Y.J. Gong, J.S. Zhang, L. Zhan, L.L. Ma, Z.Y. Fang, R. Vajtai, X.C. Wang, P.M. Ajayan, Adv. Mater. 25 (2013) 2452–2456.
[42] R. Ohnishi, K. Takanabe, M. Katayama, J. Kubota, K. Domen, J. Phys. Chem. C 117 (2013) 496–502.
[43] H. Lee, W.Y. Choi, Environ. Sci. Technol. 36 (2002) 3872–3878.
[44] J.H. Zhou, C.Y. Deng, S.H. Si, Y. Shi, X.L. Zhao, Electrochim. Acta 56 (2011) 2062–2067.
[45] H.L. Guo, X.F. Wang, Q.Y. Qian, F.B. Wang, X.H. Xia, ACS Nano 3 (2009) 2653–2659.